PHYSICAL REVIEW B **83**, 115421 (2011)

Coherent injection and control of ballistic charge currents in single-walled carbon nanotubes and graphite

R. W. Newson,[1] A. A. Green,[2] M. C. Hersam,[2] and H. M. van Driel[1]

[1]*Department of Physics, Institute for Optical Sciences, University of Toronto, 60 St. George Street, Toronto, Ontario, Canada M5S 1A7*
[2]*Department of Materials Science & Engineering and Department of Chemistry, Northwestern University, 633 Clark Street, Evanston, Illinois, USA 60208*

(Received 11 October 2010; revised manuscript received 9 January 2011; published 11 March 2011)

We report results from a comprehensive set of experiments to study coherently controlled electrical current injection in single-walled carbon nanotubes (SWNTs) and graphite. Photocurrents were injected at room temperature through the quantum interference of single- and two-photon absorption pathways induced by 150-fs optical pulses with 660–980 and 1320–1960-nm central wavelengths, respectively, and with maximum intensities of 10 and 0.15 GW cm^{-2}, respectively. Detection of the photocurrents was achieved via the emitted terahertz radiation. For bulk graphite samples and collinearly polarized 750- and 1500-nm pulses incident along the c axis, injected current densities up to 12 kA cm^{-2} have been observed just under the surface, independent of crystal azimuthal orientation and comparable to those generated in InP or GaAs. Current densities are ∼5 times smaller for cross-polarized pulses. A vertically aligned forest of carbon nanotubes (tube diameters ∼2.5 ± 1.5 nm) illuminated with 700- and 1400-nm pulses collinearly polarized along the alignment direction yields a maximum current of 8 nA per tube (current density of 35 kA cm^{-2}). Terahertz emission drops by only 3.5 times after 90° sample rotation about the normal, which is explained in terms of an imperfect alignment distribution (angular spread ∼19.5°) and sample birefringence. Unaligned arc discharge and HiPco SWNTs with diameters of 1.44 ± 0.15 and 0.96 ± 0.15 nm, respectively, were sorted into semiconducting and metallic tubes. Photocurrents injected with collinearly polarized 750- and 1500-nm pulses in such semiconducting SWNTs showed peak current magnitudes similar to those in the aligned nanotubes, while metallic tubes yielded currents at least ten times smaller. Semiconducting SWNT currents showed spectral features as the second-harmonic wavelength varied from 660 to 980 nm, which were more consistent with current injection based on band-band transitions than on excitonic absorption effects.

DOI: 10.1103/PhysRevB.83.115421 PACS number(s): 73.63.Fg, 78.67.Ch, 42.65.Re, 81.05.uf

I. INTRODUCTION

Considerable research attention has been devoted to carbon nanostructures in recent years due to their unique physical, optical, and electronic properties as well as their potential applications.[1–12] Graphene, a single layer of carbon atoms arranged in a hexagonal or honeycomb lattice, has remarkable optical[2] and electronic[3,4] properties and has already seen applications as a photodetector[5] and an ultrafast saturable absorber for passive laser mode locking.[6] Single-walled carbon nanotubes (SWNTs), essentially rolled-up graphene, have their own novel properties[7,8] including exceptionally high electron mobility and have been integrated into field-effect transistor designs[9,10] and used in logic circuits.[11,12] The most common method for the generation or detection of an electrical current in these structures is through the use of physically contacted electrodes.[13–15] However, the difficulty of making reliable contacts often hinders system characterization and performance.[16] The use of noncontact methods for generating electrical currents can overcome these obstacles as well as can allow the interfacing of photonics and nanoelectronics.[17,18] Optical coherence control is a well-known method to inject significant current densities in bulk and quantum well semiconductors.[19–24] In one such configuration, quantum interference between two optical absorption processes leads to the development of spin or charge currents, depending on beam polarization.[25,26] The photocurrent magnitude and direction can be controlled by varying the phase difference between the two beams. In the case of electrical current injection excited by subpicosecond pulses, the time-varying currents generate terahertz (THz) radiation that is easily detected.[21–23] Hence, both generation and detection methods are noncontact in nature.

Král and Tománek[27] and Mele *et al.*[28] showed theoretically that it is possible to inject photocurrents in graphene and SWNTs via interference of single-photon absorption (SPA) and two-photon absorption (TPA) processes.[27,28] Recently, we reported preliminary observations of such coherently controlled currents in bulk graphite and vertically aligned carbon nanotubes.[29] More recently, Sun *et al.* have observed related currents in multilayer epitaxial graphene.[30]

Here, we present results from a more comprehensive experimental study of coherently controlled current injection in bulk graphite and various types of carbon nanotubes. Samples are illuminated simultaneously by 1320–1960 nm (leading to TPA) and 660–980 nm (leading to SPA) 150-fs optical pulses at room temperature. We report on the maximum current densities injected as well as the dependence of the photocurrents on crystal orientation and optical pump polarization. For an aligned forest of mixed semiconducting and metallic nanotubes with a relatively wide diameter distribution, these results are compared with a model based on the tube alignment distribution and sample birefringence. For unaligned arc discharge and HiPco single-walled nanotube films sorted by electronic type (semiconducting vs metallic), the narrower diameter distributions yield more information from the photocurrent dependence on pump wavelength. This is meant to determine the role of excitons in this nonlinear optical process, motivated by the major contribution of excitons in linear optical absorption.[31]

In Sec. II, the background theory is presented. A simplified discussion on direct-gap semiconductors leads to the extension for graphene, graphite, and SWNTs. The role of excitons on the injection current is considered. Sec. III contains a detailed account of the fabrication and characterization of the samples used. In Sec. IV, we first outline the experimental setup and then discuss the results from bulk graphite, the vertically aligned nanotube forest, and the unaligned sorted nanotube thick films. A summary of the results and a closing perspective appear in Sec. V.

II. THEORY

A. Direct-gap semiconductors

Coherently controlled injection photocurrents have been studied extensively in several direct-gap semiconductors.[20,21,32–34] A ballistic electric current is typically optically injected through the quantum interference of two absorption pathways: SPA of a beam at frequency 2ω and TPA of a beam at frequency ω. Macroscopically, the injection current can be understood as a third-order nonlinear process[35] represented by a fourth rank purely imaginary third-order injection tensor $i\overleftrightarrow{\eta}$. For monochromatic fundamental and second-harmonic beams connecting valence- and conduction-band states, the local injected current density is dc in nature and can be expressed as[20]

$$\dot{\mathbf{J}} = i\overleftrightarrow{\eta}(0;\omega,\omega,-2\omega) : \mathbf{E}^{\omega}\mathbf{E}^{\omega}\mathbf{E}^{-2\omega} + \text{c.c.} \tag{1}$$

where $\mathbf{E}^{\omega}$ and $\mathbf{E}^{-2\omega}$ represent the complex field amplitudes of the fundamental and second-harmonic beams, respectively. Absorption of the 2ω beam is expressed through the linear absorption coefficient $\alpha_{2\omega}$. Absorption of the ω beam is expressed through an effective absorption coefficient $\alpha_{\omega}^{\text{eff}}$ that is a combination of nonlinear and linear absorptions and is defined by $\alpha_{\omega}^{\text{eff}} = \beta I_{\omega}^{0} + \alpha_{\omega}$, where β is the TPA coefficient of the material (assumed constant) and I_{ω}^{0} is the peak intensity of the ω beam. Both SPA and TPA of the ω beam are considered since this becomes relevant when expanding the discussion to carbon materials.

It is straightforward to adapt Eq. (1) for the case of pulsed excitation in which different frequency components of the pulses can lead to an ac current with components at frequency Ω. The current dynamics following optical excitation is governed by carrier ultrafast momentum relaxation, which may consist of carrier-carrier and carrier-phonon interactions as well as space-charge fields related to the separation of electrons and holes. The oscillating current will emit electromagnetic radiation, which, for subpicosecond pulse excitation, is in the THz range. The THz radiation field with frequency Ω is an integral over all possible optical frequency permutations and the depth z into the sample with thickness D,

$$\mathbf{E}_{\text{inj}}^{\text{THz}}(\Omega) \propto \int_{0}^{D} dz \int \frac{d\Omega_1}{2\pi} \int \frac{d\Omega_2}{2\pi} \dot{\mathbf{J}}(\Omega,\Omega_1,\Omega_2,z) + \text{c.c.}, \tag{2}$$

where

$$\begin{aligned}\dot{\mathbf{J}}(\Omega,\Omega_1,\Omega_2,z) &= i\overleftrightarrow{\eta}(-\Omega;\omega+\Omega_1,\omega+\Omega_2,\\ &\quad -2\omega-\Omega_1-\Omega_2+\Omega)\\ &: \mathbf{E}^{\omega}(\omega+\Omega_1,z)\\ &\times \mathbf{E}^{\omega}(\omega+\Omega_2,z)\,\mathbf{E}^{2\omega}(2\omega+\Omega_1+\Omega_2-\Omega,z)^{*}\end{aligned} \tag{3}$$

We now assume Gaussian laser pulses with central frequencies ω and 2ω, frequency bandwidths σ_{ω} and σ_{2w}, surface peak field strengths E_0^{ω} and $E_0^{2\omega}$, unit polarization vectors $\hat{\mathbf{e}}_{\omega}$ and $\hat{\mathbf{e}}_{2\omega}$, and phases at the sample surfaces ϕ_w and $\phi_{2\omega}$, respectively. It is straightforward to perform the integration and to simplify to the following expression:

$$\begin{aligned}\mathbf{E}_{\text{inj}}^{\text{THz}}(\Omega) &\propto [\overleftrightarrow{\eta} : \hat{\mathbf{e}}_{\omega}\hat{\mathbf{e}}_{\omega}\hat{\mathbf{e}}_{2\omega}^{*}]E_0^{\omega}E_0^{\omega}E_0^{2\omega}\left(\frac{1}{\sigma_{\Omega}}\right)\exp\left(\frac{-\Omega^2}{\sigma_{\Omega}^2}\right)\\ &\times(\Xi_{+}^{2}+\Xi_{-}^{2})^{1/2}\sin\left[\Delta\phi + \arctan\left(\frac{\Xi_{+}}{\Xi_{-}}\right)\right],\end{aligned} \tag{4}$$

where $\sigma_{\Omega}^2 = 2\sigma_{\omega}^2 + \sigma_{2\omega}^2$, $\Delta\phi = 2\phi_{\omega} - \phi_{2\omega}$, and Ξ_{+} and Ξ_{-} are

$$\begin{aligned}\Xi_{\pm} &= \frac{1}{2}\left(\frac{(\Delta k+\gamma)\pm(\Delta k-\gamma)}{\gamma^2+\Delta k^2}\right)\\ &\times\left\{1 - e^{\gamma D}\left[\cos(\Delta k D) \pm \left(\frac{\gamma}{\Delta k}\right)^{\pm 1}\sin(\Delta k D)\right]\right\}\end{aligned} \tag{5}$$

Here, $\Delta k = (2\omega/c)(n_{\omega} - n_{2\omega})$ represents the wave-vector mismatch in the sample, and $\gamma = \alpha_{\omega}^{\text{eff}} + \frac{1}{2}\alpha_{2\omega}$ represents the injection current decay into the sample due to optical absorption. If the sample can be approximated as a semi-infinite slab such that $D \to \infty$, Eq. (4) simplifies to

$$\begin{aligned}\mathbf{E}_{\text{inj}}^{\text{THz}}(\Omega) &\propto [\overleftrightarrow{\eta} : \hat{\mathbf{e}}_{\omega}\hat{\mathbf{e}}_{\omega}\hat{\mathbf{e}}_{2\omega}^{*}]E_0^{\omega}E_0^{\omega}E_0^{2\omega}\left(\frac{1}{\sigma_{\Omega}}\right)\exp\left(\frac{-\Omega^2}{\sigma_{\Omega}^2}\right)\\ &\times(\gamma^2+\Delta k^2)^{-1/2}\sin[\Delta\phi + \arctan(\Delta k/\gamma)].\end{aligned} \tag{6}$$

The current depends sinusoidally on the relative phase of the two pump beams via the phase parameter $\Delta\phi$.

In order to determine the dependence of the injection current on a material's geometry or the pump beam polarizations, a proper laboratory frame of reference must be defined. Let the Z axis be along the sample surface normal such that the sample surface is in the XY plane. We take the 2ω beam to be linearly polarized along the X axis, while the ω beam is linearly polarized at an angle θ to the X axis in the XY plane. Therefore, $\theta = 0$ represents copolarized pump beams, while $\theta = \pi/2$ represents orthogonal pump beams.

For our experiments on carbon nanostructures, zinc-blende semiconductors, such as InP and GaSb are used as a reference. For these materials, the generalized current injection tensor has 21 nonzero elements, only four of which are independent.[36] For (100)-oriented crystals under normal incidence of two pump beams (ω, 2ω), the number of independent tensor elements reduces to 3. If the principal crystal axes (x and y) are aligned along the X and Y axes, one obtains from Eqs. (4) and (6):

$$\begin{bmatrix} E_{\text{inj},X}^{\text{THz}} \\ E_{\text{inj},Y}^{\text{THz}} \end{bmatrix} \propto \begin{bmatrix} \eta_{xxxx}\cos^2\theta + \eta_{xyyx}\sin^2\theta \\ \eta_{xyxy}\sin 2\theta \end{bmatrix} \tag{7}$$

Values for the current injection tensor elements as a function of wavelength for several such semiconductors are given elsewhere.[32]

B. Graphene and graphite

Although graphite is a semimetal and graphene is a zero-gap semiconductor, injection currents can still be generated using ω and 2ω pump beams. For both graphene and graphite, light can be absorbed at any wavelength, and, therefore, there will always be SPA of both pump beams. This may reduce the ω beam power available for TPA, but nevertheless, injection currents are given by Eqs. (4) and (6) and should still be measurable.

Since both graphene and graphite have a hexagonal crystal structure, the generalized injection tensor has 21 nonzero elements, only 10 of which are independent.[36] The situation is greatly simplified by considering only normal sample incidence, whereby the laser propagation direction (Z axis) is parallel to the crystal c axis. In this case, the tensor product in the square brackets of Eqs. (4) and (6) reduces to that in Eq. (7), with the additional relation $\eta_{xyxy} = \frac{1}{2}(\eta_{xxxx} - \eta_{xyyx})$ so that

$$\begin{bmatrix} E^{\mathrm{THz}}_{\mathrm{inj,X}} \\ E^{\mathrm{THz}}_{\mathrm{inj,Y}} \end{bmatrix} \propto \begin{bmatrix} \eta_{xxxx}\cos^2\theta + \eta_{xyyx}\sin^2\theta \\ \frac{1}{2}(\eta_{xxxx} - \eta_{xyyx})\sin 2\theta \end{bmatrix} \tag{8}$$

In fact, this additional symmetry relation implies that the injection tensor has cylindrical symmetry about the c axis, and the injected current direction should not change when rotating the sample about this axis.

Mele *et al.*[28] used a tight-binding model of low-energy electronic states to develop a formalism for the coherent injection of currents in graphene and SWNTs. For graphene, the authors conclude that, if the ω beam polarization makes an angle of θ with respect to the 2ω beam polarization, the net photocurrent direction makes an angle of 2θ. This implies that $\eta_{xxxx} = -\eta_{xyyx}$. The paper does not develop a theory for bulk graphite, but predicts similar, if not exactly, the same results.

C. SWNTs

For current injection in carbon nanotubes, Mele *et al.*[28] considered low-energy excitation of a single straight SWNT. Two configurations, shown in Fig. 1, can lead to injected electrical current via quantum interference of single- and two-photon absorption processes, with the current directed along the tube axis in both cases. In the first configuration, the ω and 2ω beams are polarized along the tube axis, while in the second configuration, the 2ω (ω) beam is polarized parallel (perpendicular) to the tube axis.

In both cases, SPA of the 2ω beam couples a particular pair of valence and conduction sub-bands. TPA, on the other hand, proceeds via two steps: a transition from an initial state to an intermediate state induced by an ω photon, followed by a transition from the intermediate state to the final state. In the first configuration [Fig. 1(b)], second-order perturbation theory shows that the dominant intermediate state for the TPA of the ω light is the same as the initial or final state. Figure 1(b) illustrates the latter, wherein TPA proceeds via a virtual (energy nonallowed) transition of an ω photon followed by a second virtual transition from the intermediate (final) state to itself, with energy being conserved in the overall transition from valence to conduction band. For this configuration, one can assign an effective injection tensor element $\eta_{||}$ that depends on ω. In the second configuration [Fig. 1(c)], the dominant intermediate state for TPA is in a band whose azimuthal quantum number differs by ±1 from that of the final band. Here, TPA occurs with a virtual (energy nonallowed) transition to this intermediate state followed by a second virtual transition from the intermediate state to the final state. This configuration, represented through current injection tensor element $\eta_\perp$, is predicted to produce weaker photocurrents than the first configuration. For both semiconducting and metallic tubes, any of the many sub-bands with a nonzero band gap can participate in current injection.

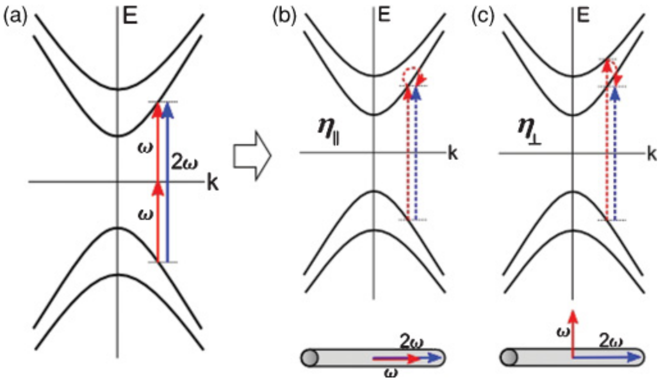

FIG. 1. (Color online) Optical transitions induced by ω and 2ω beams leading to current injection in a SWNT. (a) Energy picture. (b) Illustration of actual optical transition paths (note dashed arrows) and coupled states in the case where both beams are polarized parallel to the tube axis; (c) when the ω beam is polarized perpendicular to the tube axis (see text).

Consider now a single straight SWNT oriented in the XY plane at angle ψ relative to the X axis. Recall that the 2ω beam is polarized along the X axis while the ω beam polarization makes an angle of θ with the 2ω beam polarization. In this case, Eqs. (4) and (6) predict an angular dependence of the THz radiation given by

$$\begin{bmatrix} E^{\mathrm{THz}}_{\mathrm{inj,X}} \\ E^{\mathrm{THz}}_{\mathrm{inj,Y}} \end{bmatrix} \propto [\eta_{||}\cos^2(\theta-\psi) + \eta_\perp \sin^2(\theta-\psi)] \times \cos\psi \cdot \begin{bmatrix} \cos\psi \\ \sin\psi \end{bmatrix}. \tag{9}$$

In our experiments, ensembles of carbon nanotubes are studied. Samples are solid films containing a very large number of carbon nanotubes and possibly a large number of chiralities. In some samples, the nanotubes may be mostly aligned in one direction, while in other samples, individual nanotube orientation is random. An alignment function is defined by $A(\psi)$, which represents the fraction of nanotubes in the ensemble sample aligned between ψ and $\psi + d\psi$ in the XY plane. Since $\int_0^\pi \mathrm{A}(\psi)d\psi = 1$, the isotropic case (no preferential tube alignment) is represented by $A(\psi) = 1/\pi$. For an ensemble sample of rigid SWNTs, Eq. (9) must be averaged over all ψ to obtain

$$\begin{bmatrix} E^{\mathrm{THz}}_{\mathrm{inj,X}} \\ E^{\mathrm{THz}}_{\mathrm{inj,Y}} \end{bmatrix} \propto \int_0^{\pi} [\eta_{||} \cos^2(\theta-\psi) + \eta_{\perp} \sin^2(\theta-\psi)] \times \cos\psi \cdot \begin{bmatrix} \cos\psi \\ \sin\psi \end{bmatrix} \cdot \mathrm{A}(\psi) d\psi. \tag{10}$$

In reality, carbon nanotubes are not rigid. A long single nanotube can be aligned at a mean angle ψ' but can contain enough bends such that its shorter tube segments are aligned at a distribution of angles around ψ'. In this case, each nanotube can be approximated as a chain of small rigid tube *segments*, and the alignment distribution represents the angular distribution of segments in the sample. In addition, an electrical current can change direction as the nanotube bends. For an ensemble nanotube sample, this results in an effective scattering of any injected currents. If the alignment distribution of tube segments within the average nanotube is considered Gaussian, then,

$$B(\psi',\psi) = \frac{1}{\psi_s\sqrt{\pi}} \sum_{j=-\infty}^{\infty} (-1)^j \exp\left(-\frac{(\psi'-\psi-j\pi)^2}{\psi_s^2}\right), \tag{11}$$

where ψ is the mean alignment angle of the tube and ψ_s is the bend scattering angle. The $(-1)^j$ prefactor is necessary to preserve the net current direction. Considering this bend scattering, Eq. (10) takes the form

$$\begin{bmatrix} E^{\mathrm{THz}}_{\mathrm{inj,X}} \\ E^{\mathrm{THz}}_{\mathrm{inj,Y}} \end{bmatrix} \propto \int_0^{\pi} [\eta_{||} \cos^2(\theta-\psi) + \eta_{\perp} \sin^2(\theta-\psi)]\ \cos\psi \times \int_0^{\pi} A(\psi')B(\psi',\psi) \cdot \begin{bmatrix} \cos\psi' \\ \sin\psi' \end{bmatrix} d\psi' d\psi. \tag{12}$$

Note that in the special case of rigid sticklike nanotubes, $\psi_s \rightarrow 0$ and $\mathrm{B}(\psi',\psi)$ becomes a Dirac δ function centered at angle $\psi' = \psi$, simplifying Eq. (12) to Eq. (10).

For simplicity, we assume that the overall alignment distribution is also Gaussian such that

$$A(\psi) = \frac{1}{\psi_a\sqrt{\pi}} \sum_{j=-\infty}^{\infty} \exp\left(-\frac{(\psi-\psi_0-j\pi)^2}{\psi_a^2}\right), \tag{13}$$

where ψ_0 is the mean alignment angle of the sample and ψ_a is the angular width. For further discussion regarding the choice of this distribution function, see Sec. III B. $\psi_0 = \pi/2$ represents the case of nanotubes generally aligned along the Y axis, while $\psi_0 = 0$ represents tubes generally aligned along the X axis. For the case of perfect alignment, $\psi_a,\psi_s \rightarrow 0$ and $A(\psi)$ becomes a Dirac δ function centered at $\psi = \psi_0$, simplifying Eq. (10) to Eq. (9).

For the isotropic case of $\psi_a \rightarrow \infty$ and $A(\psi) = 1/\pi$, Eq. (12) simplifies to

$$\begin{bmatrix} E^{\mathrm{THz}}_{\mathrm{inj,X}} \\ E^{\mathrm{THz}}_{\mathrm{inj,Y}} \end{bmatrix} \propto \frac{1}{8} \exp\left(-\frac{\psi_s^2}{4}\right) \cdot \times \begin{bmatrix} (3\eta_{||}+\eta_{\perp})\cos^2\theta + (\eta_{||}+3\eta_{\perp})\sin^2\theta \\ (\eta_{||}-\eta_{\perp})\sin 2\theta \end{bmatrix}, \tag{14}$$

and simplifies even further to

$$\begin{bmatrix} E^{\mathrm{THz}}_{\mathrm{inj,X}} \\ E^{\mathrm{THz}}_{\mathrm{inj,Y}} \end{bmatrix} \propto \frac{1}{8} \begin{bmatrix} (3\eta_{||}+\eta_{\perp})\cos^2\theta + (\eta_{||}+3\eta_{\perp})\sin^2\theta \\ (\eta_{||}-\eta_{\perp})\sin 2\theta \end{bmatrix}, \tag{15}$$

in the rigid sticklike approximation. In this case, the effect of bend scattering is to simply reduce the net current magnitude.

For the case of perfect alignment along the Y axis ($\psi_a,\psi_s \rightarrow 0, \psi_0 = \pi/2$), it is not surprising that there is no current injected, since the 2ω beam must have a nonzero component along the tube axis in both configurations. For the case of perfect alignment along the X axis ($\psi_a,\psi_s \rightarrow 0, \psi_0 = 0$), Eq. (12) simplifies to

$$\begin{bmatrix} E^{\mathrm{THz}}_{\mathrm{inj,X}} \\ E^{\mathrm{THz}}_{\mathrm{inj,Y}} \end{bmatrix} \propto \begin{bmatrix} \eta_{||}\cos^2(\theta) + \eta_{\perp}\sin^2(\theta) \\ 0 \end{bmatrix}. \tag{16}$$

In Sec. IV, experimental results are presented to test the validity of this model by varying several of these geometrical parameters.

The pump frequency dependence of the injection current across sub-band gap E_{mm} in a SWNT can be obtained by using the Mele *et al.*[28] perturbation calculation for the rate of change of the third-order occupation probability when the pump fields are polarized along the tube axis. It is straightforward to show that[37]

$$\eta_{||}(\omega) \propto \frac{E_{\mu\mu}}{\omega^4}\sqrt{(2\hbar\omega)^2 - E_{\mu\mu}^2}. \tag{17}$$

D. Possible role of excitons in current injection in SWNTs

Excitons in a SWNT are known to possess large binding energies and to dominate linear optical absorption characteristics.[31,38] With strong light absorption into bound exciton states, it is valid to inquire about the influence of excitons on current injection. Recently, Sames *et al.*,[33] Marti *et al.*,[23] and Rumyantsev and Sipe[39] have shown how coherent control involving exciton states with different spatial symmetry in bulk and quantum well semiconductors can lead to the generation of ultrafast ac currents. In particular, $1s$ and $2p$ excitons are excited by TPA of ω and SPA of 2ω beams. The exciton states are separated by $\hbar\Omega_{1s-2p}$, which can be small compared with pump bandwidths. Hence, both exciton states are accessible by one set of pump pulses whose center frequencies differ by a factor of 2. The ac current leads to a THz emission spectrum shifted by Ω_{1s-2p} from the dc current injection case. However, the most important difference is that the phase parameter $\Delta\phi$ now controls the phase of the current and not the current magnitude. The direction of the ac current depends on the exciton wave functions.

Here, we only briefly outline the various types of excitons that might possibly contribute to an ac current injection. For each sub-band transition between valence band μ and conduction band μ', a set of excitons exists with excitation energies below the corresponding sub-band energy gap $E^{S,M}_{\mu\mu'}$, where the superscript is either S or M for semiconducting or metallic. There are a variety of excitons that exist for each sub-band transition, with different symmetry and hydrogenic order.

Carriers can be excited in SWNTs by low-energy photons around the K and K' regions in the Brillouin zone. An exciton in the same region is labeled an $A-$symmetry exciton. Such excitons are further categorized by their wave-function symmetry under C_2 (180°) rotation around the axis perpendicular to the tube axis. A_1 (A_2) excitons are symmetric (antisymmetric) under this rotation. In addition, each exciton type possesses a set of hydrogenlike orbitals. They are labeled by ν (the *hydrogenic order*), where $\nu = 0$ represents the lowest state (similar to a 1s orbital), $\nu = 1$ represents the next higher state (similar to a 2p orbital), etc.

The absorption properties of excitons depend on light polarization and nanotube chirality. Barros *et al.*[40] have determined that SPA and TPA selection rules for excitons in SWNTs do not rely only on simple symmetry arguments. For light polarized along the tube axis, only A_2 (A_1) excitons are optically active for SPA (TPA) absorption. Unique exciton energies are labeled by $E_{\mu\mu}(A^{\nu}_{1,2})$. For SPA, even values of ν (0, 2, 4, ...) lead to the strongest absorption, as one may expect since they are symmetric about reflection in the tube axis. However, with the exception of zigzag tubes, excitons with odd values of ν (1, 3, 5, ...) still do have a nonzero (albeit weak) absorption despite their antisymmetric reflection property. For TPA, the reverse is the case, where odd values of ν are associated with strong absorbers while even values of ν are associated with weak (zero in zigzag tubes). Figure 2 shows a diagram of the allowed exciton energies associated with a fundamental energy gap E_{11} for both SPA and TPA.[40] The energies $E_{11}(A^{\nu}_1)$ and $E_{11}(A^{\nu}_2)$ are usually very similar at each value of ν but not exactly the same.

For SWNTs, the intuitive extension of the generation of an ac current in a III–V semiconductor would be to excite A^0_2 excitons with SPA and A^1_1 excitons with TPA simultaneously (see Fig. 2) with the same set of optical pump pulses. However, the two exciton states are energetically separated by much more than the optical pulse bandwidth for pulses of duration >100 fs. The other possibility would be to excite A^1_1 excitons with TPA but to simultaneously excite A^1_2 excitons with SPA. The states are energetically separated by tens of meV, comparable to the optical pulse bandwidths typically used.

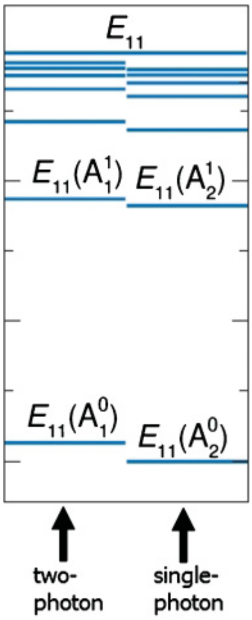

FIG. 2. (Color online) Diagram of single- and two-photon active excitons associated with an E_{11} transition.[38]

Since the A^1_1 and A^1_2 excitons have the same symmetry about reflection in the tube axis but different symmetry under C_2 rotation around the axis perpendicular to the tube axis, their excitation should only result in a circular ac current around the nanotube and not a linear ac current along the tube axis. This oscillating circular current would create an oscillating magnetic dipole moment along the tube axis. Magnetic dipole radiation would result, although the magnitude is usually small, and the polarization of the emitted THz pulse would be perpendicular to the magnetic moment (tube axis). Overall, we do not expect to see significant influence of excitons on current injection in SWNTs.

III. SAMPLES

A. Graphite

The graphite material used was freshly cleaved natural flake graphite, acquired from Asbury Carbons, with a purity of 99.59% carbon.

B. Vertically aligned nanotube forest

The aligned carbon nanotube sample is a chemical vapor deposition (CVD)-grown forest of carbon nanotubes (V-SWNTs). Growth process parameters, such as the catalyst particle size, gas species, temperature, pressure, etc., can control the distribution of nanotube diameters to some degree. While SWNTs are preferentially grown, there are also multiwalled nanotubes present in the sample. Most SWNTs are *bundled*, meaning they are bonded wall to wall with other SWNTs via van der Waals forces. The nanotubes grow tightly packed, which helps them stand vertically on the substrate and creates a high degree of alignment throughout the sample. The approximate tube diameter distribution is 2.5 ± 1.5 nm with tubes growing to a height of 150–200 μm. Figure 3 shows scanning electron microscopy (SEM) images of the side facet of the nanotube forest at two different magnifications. The side facet is optically smooth and of sufficient size to receive a focused laser beam.

While the nanotubes are well aligned, they are not perfectly aligned. If the tubes clearly in focus in Fig. 3(b) are divided into small rigid segments, each segment can be characterized by the angle it makes with the substrate ψ. A histogram of such tube segment angles is shown in Fig. 4 for a 50-nm segment length and 7.5° bin size. From the SEM image, this segment length appears small enough to represent the approximate length over which a nanotube or nanotube bundle remains straight. The histogram approximates the sample's alignment distribution $A(\psi)$ (see Sec. II C). A Gaussian fit is also shown representing Eq. (12) with angular width $\psi_a = 19.5^\circ \pm 0.9^\circ$.

C. Unaligned sorted nanotube thick films

The large mean diameter and diameter distribution of the nanotubes in the aligned sample make a detailed investigation

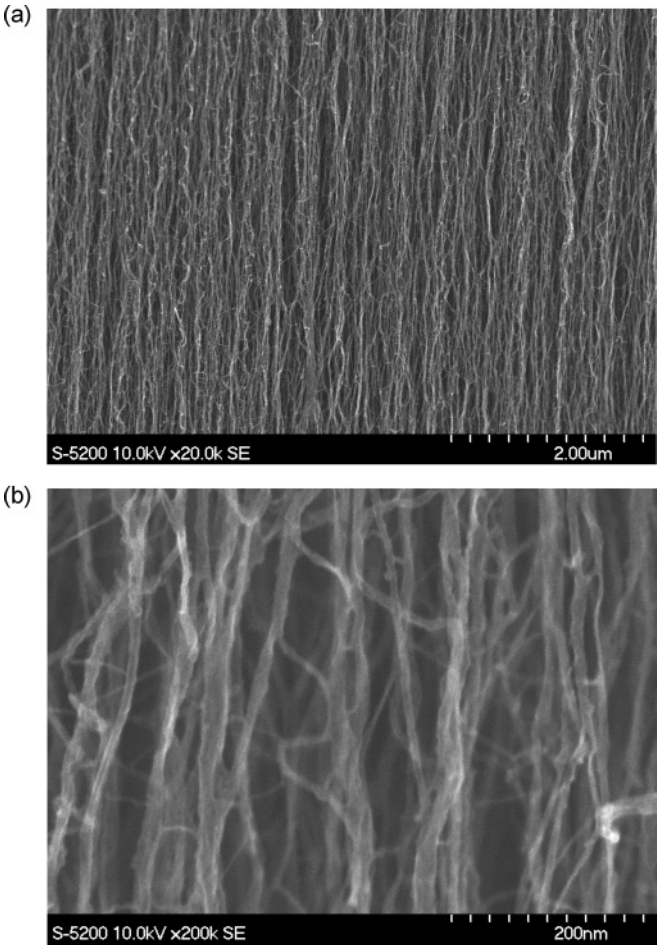

FIG. 3. Images of the side facet of the vertically aligned forest of carbon nanotubes, taken at (a) 20 000× and (b) 200 000× with a Hitachi S-5200 SEM.

of current injection difficult. Therefore, we have explored a variety of sorted samples (X-SWNT) with different mean tube diameters, and with tighter diameter distributions, sorted by electronic type (metallic vs semiconducting). The details of the sorting procedure along with the associated supplementary materials are given elsewhere.[41,42] Ensemble samples of SWNTs are produced by arc discharge or HiPco methods and are suspended in a 1% weight-to-volume ratio aqueous solution of sodium cholate surfactant. Density gradient ultracentrifugation of the nanotubes is then performed in gradients containing anionic surfactants tailored to isolate nanotubes of the desired diameter and electronic character. The sorted nanotube dispersions are subsequently dialyzed to remove the density gradient medium iodixanol and are drip dried onto a glass substrate to form opaque films of ∼10-μm thickness.

Absorbance measurements on the samples in solution and subsequently on the films show resonance peaks corresponding to known optical transitions for each chirality of nanotube within each sample. From the magnitude of these peaks, one can estimate the diameter distribution of each sample. While it is known that a weak chirality dependence of the nanotube oscillator strength leads to an ∼10% variation in the absorption intensity in the same $2n + m$ family,[43] it is common to neglect this dependence in the diameter distribution determination.[44–46] Samples are divided into arc discharge samples with diameter distribution 1.44 ± 0.15 nm and HiPco samples with diameter distribution 0.96 ± 0.14 nm. Each of these types are split into those containing mostly (>96%) semiconducting tubes, mostly (>91%) metallic tubes, and the natural mixture (∼67% semiconducting, ∼33% metallic) of tubes.[47,48] A plot of the absorption spectra (in solution) of these six samples is shown in Fig. 5.

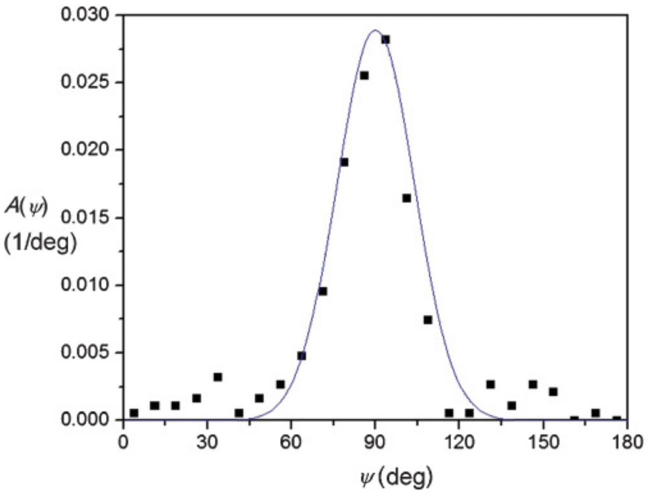

FIG. 4. (Color online) Histogram of 50-nm long tube segment angles measured from Fig. 3(b) (black squares) and Gaussian fit function with $\psi_a = 19.5^\circ$ (blue curve).

The peaks seen in Fig. 5 represent the lowest exciton states (A_2^0) of the various band-band transitions in each nanotube chirality present in the sample. For the arc discharge nanotubes in Fig. 5(a), the broad absorbance peak observed around 1 μm corresponds to the collective absorption from the exciton states of the second semiconducting transition of all the semiconducting nanotubes in the sample. The peak corresponding to the fundamental semiconducting gap is out of range, at around 1.8 μm. The peak observed near 700 nm corresponds to the first gapped metallic transition. For the HiPco nanotubes, absorption resonances are more separated, and almost every peak can be attributed to a specific nanotube chirality. In Fig. 5(b), fundamental semiconducting transitions are shown for wavelengths >870 nm, while second semiconducting resonances appear for wavelengths 550–900 nm and first metallic resonances appear for wavelengths 400–650 nm.

The method of drip-drying suspended nanotube solutions onto glass substrates does not create a uniformly thick film but rather a circular film thickest at its edges (a crater shape). However, since the films are several millimeters in diameter, regions of sufficient thickness and flatness on the order of the incident laser spot size (∼100 μm) can be identified. This identification is made by mapping each film's surface height profile using an optical surface profiler. For our experiments, an optimal spot on each film is located, and the pump beams are incident on that spot for each measurement for consistency. The thickness of the film at this spot is taken from the surface profile. Table I lists all carbon nanotube samples used in the experiments.

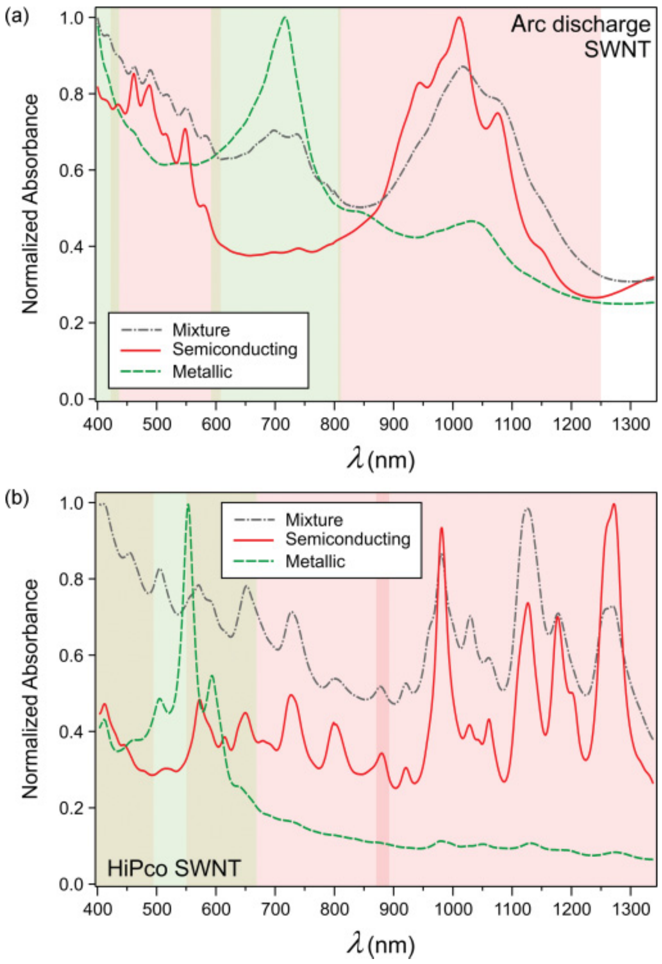

FIG. 5. (Color online) Normalized absorbance spectra for unaligned (a) arc discharge SWNT sample ($d_t = 1.44 \pm 0.15$ nm); and (b) HiPco SWNT sample ($d_t = 0.96 \pm 0.14$ nm) in solution after sorting.

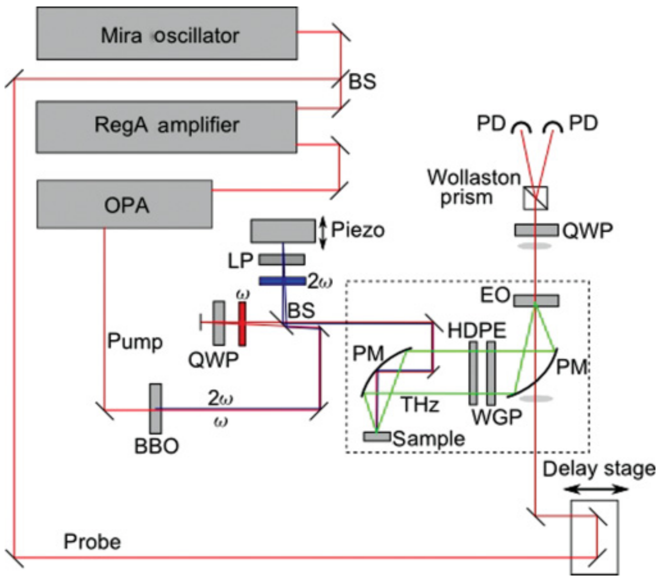

FIG. 6. (Color online) Diagram of the experimental setup for coherent control of photoinjected currents.

IV. COHERENT CONTROL EXPERIMENTS

Figure 6 shows the experimental setup used to coherently inject electrical currents into the samples. A commercial 250-kHz Ti:sapphire oscillator/amplifier operating at 810 nm is used to pump an optical parametric amplifier (OPA) yielding 150-fs pulses, tunable between 1320 and 1960 nm (ω beam) with an average power up to 55 mW. A 1.5-mm-thick β barium borate (BBO) crystal converts part of the ω beam to 660–980-nm light (2ω beam) with an average power of up to 1 mW. Control of the relative phase parameter $\Delta\phi = 2\phi_\omega - \phi_{2\omega}$ is achieved via piezocontrol of the length of the 2ω arm of a Michelson interferometer, which also contains a linear polarizer (LP) to ensure a constant linear polarization. The ω arm of the interferometer has a quarter-wave plate (QWP) for control over the linear polarization state of the ω beam. The pump beams are focused onto samples at normal incidence and at room temperature. Average powers at the sample surface varied between 12 and 33 mW for the ω beam and between 0.3 and 0.5 mW for the 2ω beam, depending on wavelength. A spot size of 100-μm full width at half maximum generates maximum peak focused intensities of 10 and 0.15 GW cm^{-2} (for wavelengths of 1400 and 700 nm, respectively). These intensities are well below the damage threshold of the samples.

The THz radiation emitted by the photocurrents is collected and is focused by a pair of 5-cm diameter gold off-axis parabolic mirrors onto a 500-μm thick (110)-oriented ZnTe electro-optic (EO) crystal. Between these parabolic mirrors is

TABLE I. Table of carbon nanotube samples.

Sample code	Fabrication method	Electronic type	Diameter distribution (nm)	Length distribution (μm)	Sample thickness (μm)
V-SWNT	CVD	Mixed	2.5 ± 1.5	150–200	∞
AD S-X-SWNT	AD[a]	*S*[b]	1.44 ± 0.15	0.1–2	18
AD M-X-SWNT	AD[a]	*M*[c]	1.44 ± 0.15	0.1–2	14
AD U-X-SWNT	AD[a]	Mixed	1.44 ± 0.15	0.1–2	NA[49]
CO S-X-SWNT	HiPco	*S*[b]	0.96 ± 0.14	0.1–2	7
CO M-X-SWNT	HiPco	*M*[c]	0.96 ± 0.14	0.1–2	10
CO U-X-SWNT	HiPco	Mixed	0.96 ± 0.14	0.1–2	10

[a] AD stands for arc discharge.
[b] *S* stands for semiconducting.
[c] *M* stands for metallic.

a sheet of high-density polyethylene (HDPE) to filter out pump beam light and a THz wire-grid polarizer (WGP) to ensure the proper linear THz polarization. The THz beam is contained in a Plexiglas box (dashed box in Fig. 6), from which the air is purged with dry nitrogen gas to minimize THz absorption by water vapor. The THz field is measured using EO sampling techniques employing a ZnTe crystal and a weak 810-nm probe beam from the Ti:sapphire oscillator/amplifier. The change in polarization of the probe beam is measured using a Wollaston prism and a set of balanced photodetectors (PD). The difference signal is measured using a lock-in amplifier at each probe time delay τ and represents the temporal trace of the THz pulse $\tilde{S}(\tau)$. Because of phase mismatch between THz and probe pulses, the effective bandwidth of the EO detection system is estimated to be ~3 THz. Therefore, complete time resolution of the THz pulse or associated current is not obtained; however, the peak EO signal is proportional to the peak current.

Experimentally measured THz traces $\tilde{S}(\tau)$ are not explicitly shown here, since similar detailed plots have been presented in previous work (see Fig. 2 in Ref. 29). Instead, various normalization techniques are used to best understand the magnitude of the injected currents by comparing them with those in materials previously studied. Therefore, common direct-gap semiconductors with high values of current injection tensor elements[32] are used as a reference. For most experiments, InP is used as the primary reference, but for long pump wavelengths, it is necessary to use GaSb because of its smaller electronic band gap. For simplicity, a few shorthand notations are adopted from this point forward. The peak values of the measured $\tilde{S}(\tau)$ traces over time are denoted by $\tilde{S}_{\rm max} = \max[|\tilde{S}(\tau)|]$. A temporal trace can be normalized by such a peak THz value from a reference semiconductor, such as InP, and this is defined as $\tilde{S}(\tau) = \hat{\tilde{S}}(\tau) = \tilde{S}(\tau)/\tilde{S}^{\rm InP}_{\rm max}$. Finally, the peak of this normalized temporal trace is simply written as $\tilde{S}_{\rm max} = \max(|\tilde{S}(\tau)|)$, known as the *relative peak THz amplitude*.

A. Graphite

Generation of coherently controlled photocurrents in graphite was reported previously using collinearly polarized pump beams with wavelengths of 1400 and 700 nm.[29] Here, we consider the dependence of the currents on pump beam polarization and sample orientation. In addition, the samples have a higher surface quality, yielding higher THz signal/noise and more insight into the current injection process.

For pump wavelengths of 1500 and 750 nm, the relative peak THz amplitude (compared with InP), averaged over several measurements on different spot positions and samples, is measured to be $\check{S}_{\rm max} = 0.037 \pm 0.004$. The measured value of probe beam polarization contrast $\Delta I_{pr}/I_{pr} = 10^{-5}$ translates to a peak THz electric field strength of ~30 V m^{-1}. From the known SPA coefficient[50] at 750 nm and an estimated TPA coefficient of 100 cm GW^{-1} at 1500 nm (appropriate for bulk materials with ~1-eV band gap[51]), there are expected to be ~1.8 × 10^{19} carriers/cm^3 excited by SPA (at 750 nm) and ~1.5 × 10^{18} carriers/cm^3 excited by TPA (at 1500 nm) simultaneously, just under the sample surface. Using an injection current absorption coefficient of $\gamma = \alpha_\omega^{\rm eff} + \frac{1}{2}\alpha_{2\omega} = 4 \times 10^5\ {\rm cm}^{-1}$ and a wave-vector mismatch of $\Delta k = (2\omega/c)(n_\omega - n_{2\omega}) = 5.1 \times 10^4\ {\rm cm}^{-1}$, a peak current density of ~12 kA cm^{-2} for graphite is calculated just below the sample surface. This value is estimated by a comparison with previous current density calculations in GaAs[34,52] and Si,[22] taking the different material properties, spot sizes, and THz collection optics into account. The peak current density in graphite is comparable to the ~28 kA cm^{-2} computed for bulk InP just under the sample surface. The weaker THz emission from graphite is explained, in part, by the high SPA of the ω beam (nonexistent in pure InP), which removes photons that might otherwise participate in current injection and helps create a very high injection current attenuation coefficient γ.

While it would be of interest to study the coherent control of photocurrents in graphene as well as graphite, the small size and single-atom thickness of exfoliated graphene samples available to us would not produce a measurable current density in our experiments. The single-layer thickness is a factor of ~70 smaller than the skin depth calculated above, so the injected current density would be below the detection threshold for our THz system. In addition, the apparatus would need to include a higher numerical aperture (NA) focusing lens and a camera in a confocal arrangement just to target the sample. Recent work by Sun *et al.*[30] demonstrated coherent control of injection currents in multilayer (greater than nine layers) epitaxial graphene. However, no properties of the injection current were reported different from those reported here.

For graphite and graphene illuminated by pump beams propagating parallel to the c axis, symmetry arguments dictate that current injection governed by the fourth-rank $\overleftrightarrow{\eta}$ tensor is isotropic with respect to rotation about the c axis, consistent with Eq. (8). Indeed, peak THz amplitudes measured at several orientation angles for graphite were equal to within a 5% standard error. Mele *et al.*[28] had also predicted that the injected current direction in graphene is oriented at an angle of 2θ to the 2ω beam polarization, when the ω beam polarization is at an angle of θ. In the experimental geometry used here, this implies that

$$\begin{bmatrix} E^{\rm THz}_{\rm inj,X} \\ E^{\rm THz}_{\rm inj,Y} \end{bmatrix} \propto \begin{bmatrix} \eta_{xxxx} \cos 2\theta \\ \eta_{xxxx} \sin 2\theta \end{bmatrix} \qquad (18)$$

A comparison of Eq. (18) with the general case for hexagonal crystals expressed in Eq. (8) implies that $\eta_{xxxx} = -\eta_{xyyx}$ for graphene. We tested this relation for graphite by plotting the relative peak THz amplitude with respect to pump polarization angle θ. Figure 7 shows these results for 1470- and 735-nm pump wavelengths.

Clearly, the extracted value for η_{xyyx}/η_{xxxx} for graphite differs substantially (5×) from that predicted for graphene for low photon energy excitation. This could be a result of the different band structure for graphite, assumptions made in the tight-binding model leading to isotropic bands or the higher photon energy we use, whereby higher electron states are accessed. Experiments on epitaxial graphene by Sun *et al.*[30] were unable to consider the prediction of the current direction in epitaxial graphene due to lack of independent polarization control of the two pump beams (these were kept orthogonally polarized).

The band structure for graphite is approximately linear with respect to the wave vector in the wavelength range of our

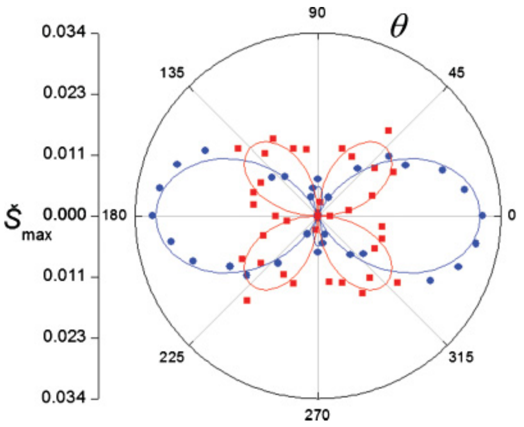

FIG. 7. (Color online) X axis (2ω beam polarization) component (blue dots) and Y axis component (red squares) of the relative peak THz amplitude from the graphite sample. Solid curves represent fits using Eq. (8) with η_{xyyx}/η_{xxxx} =−0.19. Data shown for $\theta = 190^\circ \cdots 350^\circ$ are repeated from $\theta = 10^\circ \cdots 170^\circ$.

optical source, and the linear optical properties, such as n and κ only gradually increase from 650 to 2000 nm.[50] Therefore, the pump wavelength dependence of the injected current for graphite is not expected to have significant features in this range, and no effort was made to find such.

B. Vertically aligned nanotube forest

Earlier investigations[29] achieved coherent control of photocurrents in the V-SWNT sample via the phase parameter $\Delta\phi$ and verified the expected pump intensity dependence. The magnitude of current injected using collinearly polarized 1400- and 700-nm pump beams was ∼10× smaller than those injected in InP under the same excitation conditions. Greater experimental accuracy has since yielded a better measurement of $\tilde{S}_{\max} = 0.11 \pm 0.01$, which translates to a peak THz electric field strength of ∼85 V m^{-1}. The SPA and TPA coefficients are not known for this sample, but similar values for graphite are assumed for these and the injected carrier densities. Incorporating corresponding absorption and wave-vector mismatch values (not done previously[29]), one can compute a more accurate peak current density of ∼35 kA cm^{-2} for the V−SWNT sample immediately under the surface. From the SEM images in Fig. 3, the fraction of cross-sectional area occupied by the nanotubes (packing fraction) is estimated to be no more than ∼0.2, which means that, for the particular illumination conditions, the peak injected current is ∼8 nA per nanotube, higher than initially estimated.[29]

The high degree of alignment of the nanotubes in the V-SWNT sample (see Fig. 3) should imply a significant anisotropy of the current generation process. This anisotropy was observed previously[29] by varying the sample orientation relative to collinear pump beam polarization. The injection current was maximal when the tubes were aligned parallel to the pump polarization direction ($\psi_0 = 0$) and was smaller by a factor of 3.4 ± 0.4 when the tubes were aligned perpendicular to the pump polarization direction ($\psi_0 = 90^\circ$). In Sec. II C, it was shown that, for perfect alignment ($\psi_a, \psi_s \to 0$), current generation should not be possible without a component of the 2ω beam parallel to the tube alignment direction. The tubes in the V-SWNT sample are not perfectly aligned, explaining, at least in part, why the current at $\psi_0 = 90^\circ$ is nonzero. However, the alignment analysis in Sec. III B finds that the tubes are sufficiently aligned ($\psi_a = 19.5^\circ \pm 0.9^\circ$) to question the large ratio of parallel and perpendicular current amplitudes. The reasons for this only become apparent when performing a full pump polarization analysis.

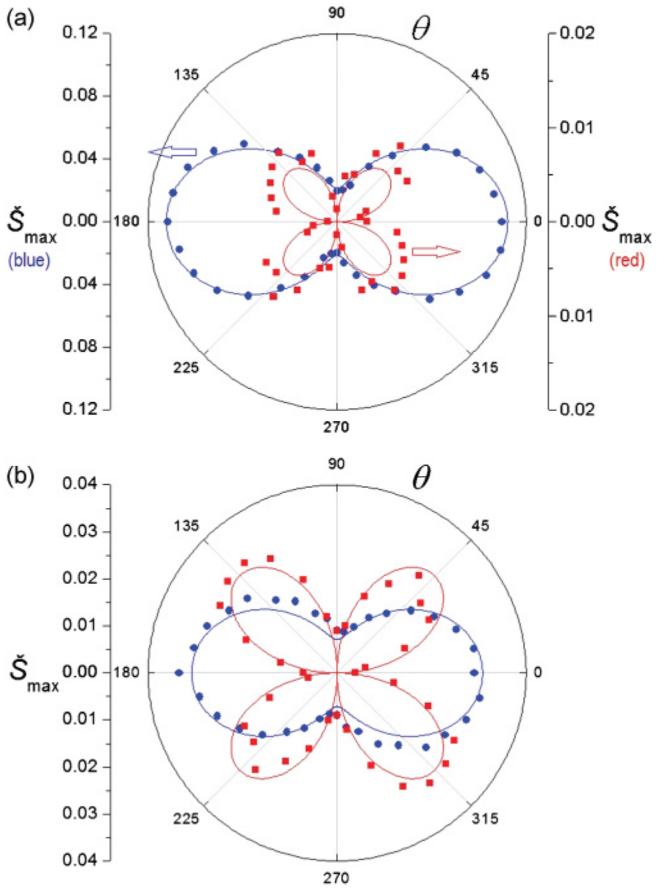

FIG. 8. (Color online) X (blue dots) and Y (red squares) axes components of the relative peak THz amplitude from the V-SWNT sample when the mean tube direction is aligned (a) along the X axis ($\psi_0 = 0$), and (b) along the Y axis ($\psi_0 = 90^\circ$). Solid curves represent fits using Eq. (19) with $\eta_\perp/\eta_\parallel$ =−0.025, $\alpha^\parallel/\alpha^\perp = 17.9$, and $t^\parallel/t^\perp = 1.01$. Data shown for $\theta = 190^\circ \cdots 350^\circ$ are repeated from $\theta = 10^\circ \cdots 170^\circ$.

As explained previously, a polarization analysis of the measured peak THz amplitude provides information on the relative values of the current injection tensor elements. For SWNTs, the two experimental configurations for current injection (Sec. II C and Fig. 1) correspond to two independent injection tensor elements, $\eta_\parallel$ and $\eta_\perp$. For the V-SWNT sample, relative peak THz amplitudes are measured for both THz components at two different alignments, $\psi_0 = 0$ (tubes aligned along the X axis/2ω beam polarization) and $\psi_0 = 90^\circ$ (tubes aligned along the Y axis). These four data sets are plotted in Fig. 8 for 1500- and 750-nm pump wavelengths, each as a function of θ, the angle between ω and 2ω beam polarizations.

It is assumed that any misalignment from the vertical growth direction occurs primarily due to the bending of the very long tubes and tube bundles, which implies that $\psi_s = \psi_a = 19.5^\circ$ in Eqs. (11) and (13). Using the theoretical model defined by Eq. (12), we attempted to find a value for $\eta_\perp/\eta_\parallel$ that provided a fit to all data in Fig. 8 as well as our previous anisotropy study.[29] Unfortunately, this was not possible until the effects of birefringence were also taken into account. For an aligned nanotube sample, the absorption should be much greater for light polarized parallel to the mean alignment direction than polarized perpendicular to it. While the linear optical properties are not known for the V−SWNT sample, birefringence can still be considered by modifying the model discussed in Sec. II C.

The Fresnel transmission coefficients at the sample surface are $t^{\parallel}_{\omega,2\omega}$ and $t^{\perp}_{\omega,2\omega}$, where the superscripts indicate polarizations parallel ($\parallel$) and perpendicular ($\perp$) to the mean tube alignment direction. In addition, the absorption coefficients $\alpha^{\text{eff}}_{\omega}$ and $\alpha_{2\omega}$ also depend on polarization. These changes to the depth dependence of the pump beams are incorporated into the unit polarization vectors $\hat{\mathbf{e}}_\omega(z)$ and $\hat{\mathbf{e}}_{2\omega}(z)$. For simplicity, it is assumed that $t^{\parallel}/t^{\perp} \equiv t^{\parallel}_{\omega}/t^{\perp}_{\omega} \approx t^{\parallel}_{2\omega}/t^{\perp}_{2\omega}$ and $\alpha^{\parallel,\perp} \equiv \alpha^{\parallel,\perp}_{\omega} \approx \alpha^{\parallel,\perp}_{2\omega}$ for the V-SWNT sample in particular. It is also reasonable to assume that $\gamma^2 \gg \Delta k^2$ since $n^{\parallel,\perp}_{\omega} \approx n^{\parallel,\perp}_{2\omega}$. These assumptions are justified later in this section. The result is that

$$\begin{bmatrix} E^{\text{THz}}_{\text{inj},X} \\ E^{\text{THz}}_{\text{inj},Y} \end{bmatrix} \propto \int_0^{\pi}\int_0^{\infty}\left(\eta_{||}\left(\hat{\mathbf{e}}_\omega(z)\cdot\begin{bmatrix}\cos\psi\\ \sin\psi\end{bmatrix}\right)^2 + \eta_\perp\left(\hat{\mathbf{e}}_\omega(z)\cdot\begin{bmatrix}-\sin\psi\\ \cos\psi\end{bmatrix}\right)^2\right)\left(\hat{\mathbf{e}}_{2\omega}(z)\cdot\begin{bmatrix}\cos\psi\\ \sin\psi\end{bmatrix}\right)dz \\ \times\int_0^{\pi} A(\psi')B(\psi',\psi)\begin{bmatrix}\cos\psi'\\ \sin\psi'\end{bmatrix} d\psi' d\psi \tag{19}$$

which is analogous to Eq. (12) except for the inclusion of the depth integral for infinite sample thickness. With these assumptions, the model contains only two unknown parameters in addition to $\eta_\perp/\eta_\parallel$, which specify the sample birefringence: $\alpha^{\parallel}/\alpha^{\perp}$ and $t^{\parallel}/t^{\perp}$. A good fit to the experimental data is achieved using this model, which is shown in Fig. 8 with fit parameters $\eta_\perp/\eta_\parallel = -0.025 \pm 0.006$, $\alpha^{\parallel}/\alpha^{\perp} = 17.9 \pm 1.6$, and $t^{\parallel}/t^{\perp} = 1.01 \pm 0.03$. Note that the absorption is highly anisotropic as one may expect.

The high degree of alignment has allowed us to measure the birefringence and relative contributions from the two current injection configurations in the V-SWNT sample. However, in obtaining this preferential alignment, access to other nanotube parameters had to be sacrificed. The tubes have large diameters and a wide distribution of diameters (and chiralities). The fundamental band gap of the 2.5-nm-diameter semiconducting SWNTs is only 0.34 eV, and such tubes will have a large number of sub-bands with larger energy gaps. With the pump wavelengths used in our experiments, sub-bands with very high azimuthal quantum numbers are excited. With so many chiralities, each with a different set of sub-band gaps, the V-SWNT sample is expected to have an almost uniform distribution of optical resonances in the optical wavelength range accessible to us. As a result, the optical properties and injection tensor elements are not expected to vary significantly, and the wavelength dependence of the peak THz amplitude for the V−SWNT sample is not expected to have any features in our range. Therefore, no spectral characteristics were sought for this sample; however, this issue motivates experiments on sorted nanotubes, considered next.

C. Unaligned sorted nanotube thick films

Although the sorted nanotubes lack alignment, they have a small mean tube diameter and a narrow diameter distribution (see Table I). A small mean tube diameter implies a large fundamental band gap, and this allows the first and/or second sub-band to selectively participate in current injection. It also reduces the number of chiralities present in a single sample so that the collective resonance peaks are sharper (see Fig. 5). In addition, sorting samples by electronic type further separates the optical resonances.

For each of the sorted samples, injection currents were observed and were controlled by varying $\Delta\phi$. Because of the well-defined absorption resonances, the peak THz amplitudes might be expected to depend on pump wavelength. A detailed analysis of the wavelength dependence appears later in this section, but we first consider collinearly polarized pump beams with wavelengths of 1500 and 750 nm, as in Secs. IV A and IV B. In this case, the peak THz amplitudes are strong for both arc discharge (0.167 ± 0.011) and HiPco (0.050 ± 0.005) semiconducting SWNT films. For metallic SWNT films, relative peak THz amplitudes are about an order of magnitude weaker than that corresponding to semiconducting samples. For mixed SWNT films, the peak THz amplitudes approximately match those of the semiconducting films, not surprising in view of the significant population of semiconducting tubes.

As with the V-SWNT sample, a polarization analysis (varying θ) should allow one to determine $\eta_\perp/\eta_\parallel$. Figure 9 shows these results for the semiconducting arc discharge sample at pump wavelengths of 1500 and 750 nm. The ratio $\eta_\perp/\eta_\parallel = -0.068 \pm 0.011$ is extracted from the fit to Eq. (14). Since the sorted samples are isotropic in their tube alignment, there is no birefringence.

The pump wavelength dependence may provide valuable insight into the mechanism for current injection in carbon nanotubes. Although it was suggested in Sec. II that excitons are unlikely to play a role in current injection, and, in particular, that axial ac currents are unlikely, we have investigated this possibility experimentally. If the injected currents are indeed due to band-band transitions, one would expect the

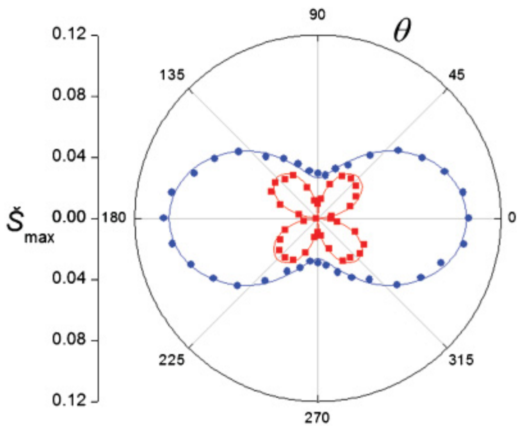

FIG. 9. (Color online) X (blue dots) and Y (red squares) axes components of the relative peak THz amplitude from the semiconducting arc discharge sample. Solid curves represent fits using Eq. (14) with $\eta_{\perp}/\eta_{\parallel} = -0.068$. Data shown for $\theta = 190^{\circ} \cdots 350^{\circ}$ are repeated from $\theta = 10^{\circ} \cdots 170^{\circ}$.

onset of the currents to occur away from the measured optical absorption peaks, since these peaks are associated with the $E_{\mu\mu}(A_2^0)$ exciton transition and not the E_{mm} band-band transition.

When the pump wavelength is changed in the OPA, other parameters change slightly as well, such as pump power, polarization, alignment, and overlap on the sample. Although every effort is made to compensate for beam misalignment, this process is difficult at wavelengths that yield low THz signals. For this reason, peak THz amplitudes $\tilde{S}_{\max}$ are normalized to those measured in the reference sample of InP or GaSb, $\tilde{S}_{\max}^{\mathrm{REF}}$, at each wavelength. However, since injection current in these semiconductors has its own wavelength dependence, it is also necessary to multiply by the theoretical peak current magnitude $S_{\mathrm{the}}^{\mathrm{REF}}$ obtained from Eq. (6) with constant pump intensities, using injection tensor element values from Ref. 32 and linear optical properties from Refs. 53 and 54. Therefore, the experimental measurements of interest are normalized as $\check{S}_{\max} = \tilde{S}_{\max}(S_{\mathrm{the}}^{\mathrm{REF}}/\tilde{S}_{\max}^{\mathrm{REF}})$. The measurements for $\check{S}_{\max}$ are shown in Fig. 10 for both arc discharge and HiPco semiconducting SWNT film samples, at second-harmonic wavelengths ranging from 660 to 980 nm. Mixed SWNT samples showed similar wavelength dependencies to those observed in the semiconducting SWNT samples. Metallic tubes are discussed later in this section.

From Fig. 10, one clearly sees several features in the injection current's wavelength dependence for both semiconducting SWNT samples. Also shown in Fig. 10, for comparison, are the absorption spectra also shown in Fig. 5 for the SWNT sample solutions. The features apparent in the injection current data seem to be broader than the absorption peaks, and the wavelengths at which the features occur do not match any obvious absorption peak wavelengths. This is significant, since the absorption peaks are due to the A_2^0 excitons and not band-band transitions.

To model the injection current theoretically, one would not only need the wavelength dependence of the injection tensor elements, but also that of the linear optical properties of the material. From Eq. (4), the general pump wavelength dependence of the peak THz amplitude is expressed by

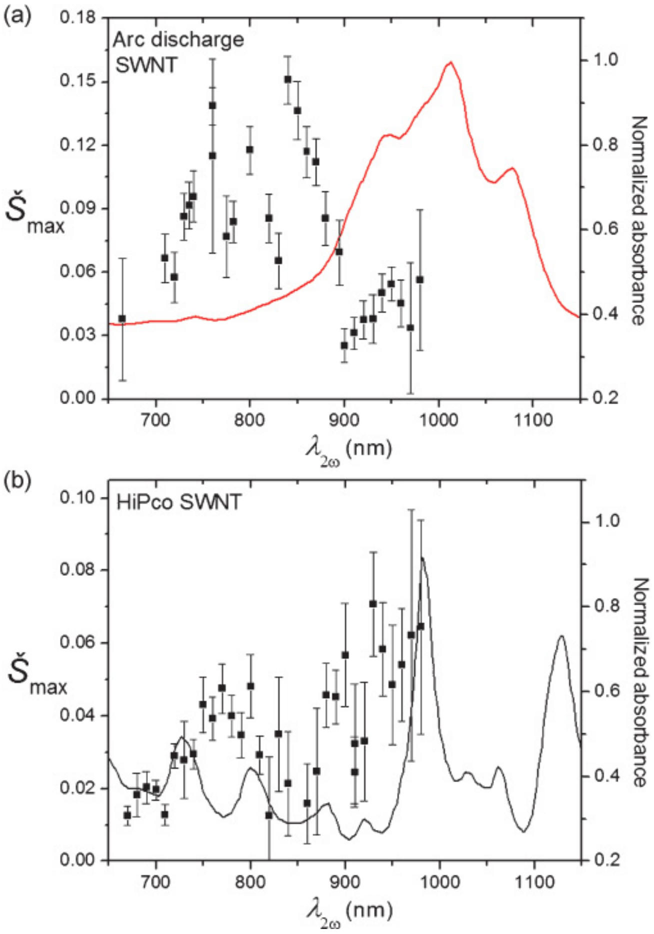

FIG. 10. (Color online) Relative peak THz amplitude (injected current magnitude) (black squares) for semiconducting nanotubes and corresponding absorbance data from SWNT solutions (red curves) as a function of second-harmonic wavelength $\lambda_{2\omega}$ for semiconducting (a) arc discharge; and (b) HiPco SWNT films.

$$E_{\mathrm{inj}}^{\mathrm{THz}} \propto \eta(\Xi_+^2 + \Xi_-^2)^{1/2}, \tag{20}$$

where η is the magnitude of an injection tensor element and the $\Xi_{\pm}$ integrals are defined by Eq. (5). For infinite thickness ($D \to \infty$),

$$E_{\mathrm{inj}}^{\mathrm{THz}} \propto \eta(\gamma^2 + \Delta k^2)^{-1/2}. \tag{21}$$

The SWNT film samples consist of a relatively low concentration of nanotubes suspended in a solidified surfactant matrix (sodium cholate). Effective linear optical properties of the films were measured by reflection and transmission spectroscopy, whereby a broadband incoherent white-light source was focused to a 1-mm-diameter spot size on each film, and both reflected and transmitted spectra were measured from 500 to 1600 nm. These measurements were used to calculate and to extrapolate $\alpha_{\omega}^{\mathrm{eff}}$ and $\alpha_{2\omega}$ in order to obtain γ for both arc discharge and HiPco semiconducting SWNT films (shown in Fig. 11). It is important to note that the SWNT film thicknesses are sufficiently large ($D \approx$ 10–20 μm), and the absorption coefficients are sufficiently small ($\gamma \approx$ 1000–5000 cm^{-1}) so that the wave-vector mismatch of the pump beams Δk is

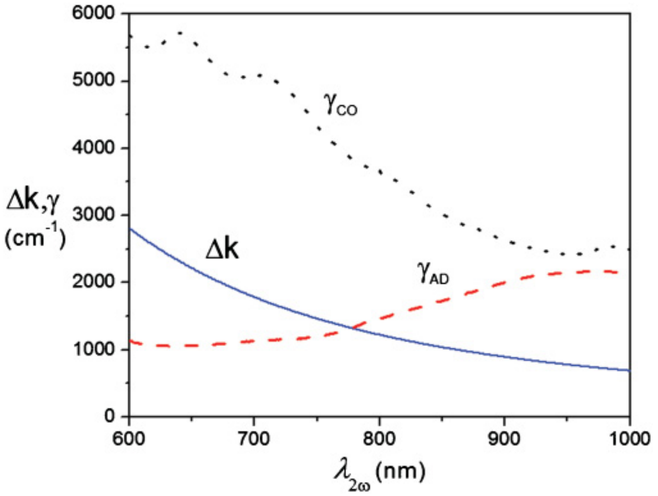

FIG. 11. (Color online) Injection current attenuation coefficient γ for arc discharge (dashed red curve) and HiPco (dotted black curve) SWNT films, as well as the wave-vector mismatch Δk for both samples (solid blue curve), each plotted as a function of second-harmonic wavelength $\lambda_{2\omega}$.

important. Refractive indices of the films were measured to be 1.5 ± 0.05. This error is much too large to obtain accurate values of $n_\omega - n_{2\omega}$, and published theoretical or experimental data for the refractive index of solidified sodium cholate do not exist. However, it is known that sodium cholate is transparent between, at least, 400 and 1700 nm, and it is reasonable to assume that the refractive index drops gradually in this range as it does with other sodium salts and most glasses. Figure 11 shows Δk as a function of second-harmonic wavelength $\lambda_{2\omega}$, assuming a refractive index dispersion of the simplest of sodium salts, NaCl.[55] It was found that even if the refractive index dispersion of BK7 glass is used,[55] a very similar effect on the current injection results.

The wavelength dependence of the injection tensor element $\eta_\parallel$ for each SWNT film is determined by Eq. (17) in conjunction with the sample's chirality distribution. From the peaks observed in the absorbance spectra, the exciton energies $E_{\mu\mu}(A_2^0)$ and the relative populations of each chirality can be measured. The sub-band energy gap $E_{\mu\mu}$ is not known with certainty for each chirality but can be computed by an empirical formula[38]

$$E_{\mu\mu} \approx E_{\mu\mu}\left(A_2^0\right) + 0.55\left(\frac{2\mu}{3d_t}\right)\log\left(\frac{9d_t}{2\mu}\right), \qquad (22)$$

where d_t is the tube diameter and $\mu = 1,2$. Using the calculated values of $E_{\mu\mu}$ along with the relative weight $g(m,n)$ for each chirality (m,n), one can evaluate the SWNT sample's total effective injection tensor element $\eta_\parallel$ as

$$\eta_\parallel(2\omega) \propto \sum_{\mu}\sum_{(m,n)} g(m,n)\frac{E_{\mu\mu}}{\omega^4}\sqrt{(2\hbar\omega)^2 - E_{\mu\mu}^2}. \qquad (23)$$

Using this $\eta_\parallel(2\omega)$ (plotted in Fig. 12) along with $\Delta k(2\omega)$and $\gamma(2\omega)$ from Fig. 11, we compute the theoretical pump wavelength dependence of the injection current in both semiconducting SWNT films from Eq. (20). This is shown in Fig. 12.

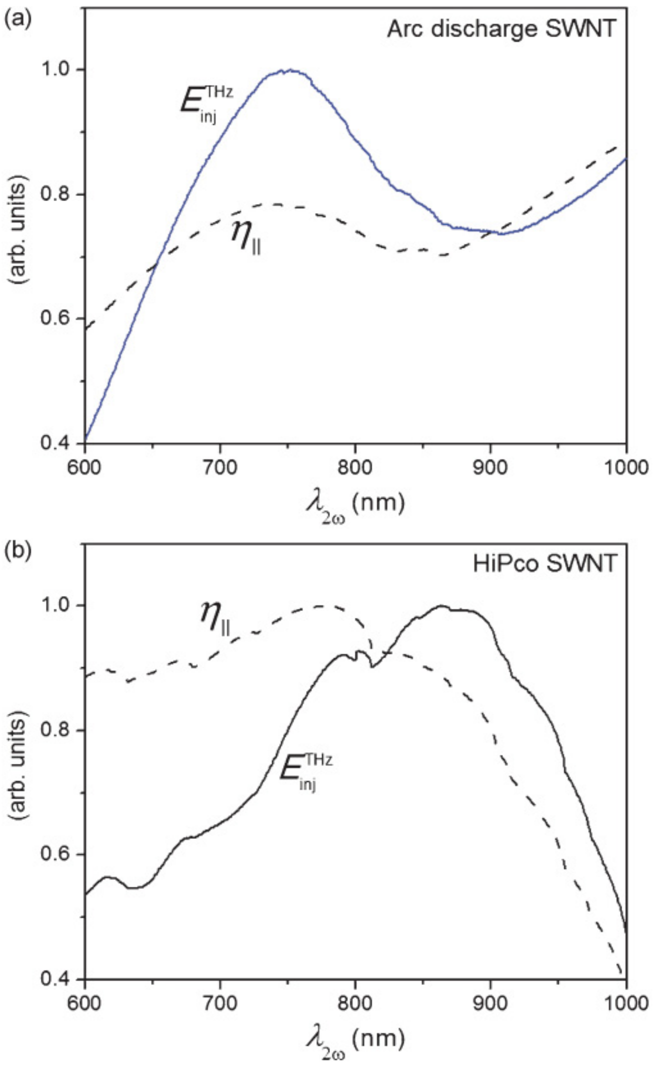

FIG. 12. (Color online) Normalized theoretical models of current injection tensor element $\eta_\parallel$ (dashed black) and total peak THz amplitude (current magnitude) $E_{\text{inj}}^{\text{THz}}$ (solid blue), each as a function of second-harmonic wavelength, for semiconducting (a) arc discharge; and (b) HiPco SWNT film samples. The $E_{\text{inj}}^{\text{THz}}$ curves are to be compared with Fig. 10.

By comparing the theory in Fig. 12 with the data in Fig. 10, one can definitely see that there are similarities in the positions and widths of the peaks. For the arc discharge sample, there clearly is a broad peak of the injection current corresponding to the E_{22}^S transition. For the HiPco sample, there are two peaks, one resulting from the high population of the (6,5) chirality, and the other mainly representing a combination of the (7,6), (8,6), (11,3), (10,3), (8,7), and (11,1) chiralities. Note that the $1/\omega^4$ dependence of the rate of change of the third-order occupation probability[28] leads to the broadening of the initially sharp band-band transition lines. Although the positions of the peaks may not exactly match the experimental data in all cases, the match is much better than if $E_{\mu\mu} \approx E_{\mu\mu}(A_2^0)$ was assumed. The difference between theory and experiment could be due to the assumptions that were necessary, such as the refractive index dispersion that influences the wave-vector mismatch or the values for the binding energies that defined $E_{\mu\mu}$. Despite this, the measurements presented here still provide evidence that the current is more likely due to band-band transitions and not excitonic effects.

For the metallic SWNT films under similar excitation conditions, the much weaker injection currents had no discernable wavelength dependence. However, peak THz amplitudes were within the noise for pump wavelengths near the edges of the measurement range where the pump power was low. The inability to inject a significant current could, in itself, be more evidence that the current injection is related to band-band transitions. In the metallic arc discharge sample, the E_{11}^M absorption peak (due to excitons) is at 700 nm and lies within the pump wavelength range. However, the band edge, theoretically shifted by about 0.26 eV, would appear at 610 nm, and this is out of the pump wavelength range. If one were able to use pump wavelengths of ~1200 and 600 nm, perhaps a much more significant injection current would be detectable.

The pump wavelength-dependent data presented in this section combined with the theoretical considerations discussed in Sec. II D provide evidence that the measured THz radiation is indeed due to ballistic injection currents based on band-band electronic transitions. The wavelength dependence of the peak THz amplitudes shows features clearly separated from the excitonic absorption lines with characteristics similar to theoretical curves calculated under the assumption that the onset of current generation occurs at the sub-band edges. Finally, with the pump bandwidths used in our experiments, the only pairs of excitonic states capable of simultaneous excitation would not have the required spatial symmetry difference that would cause an oscillating dipole along the tube axis.

V. CONCLUSIONS

The coherent control of third-order injection currents has been studied in bulk graphite and a variety of carbon nanotube samples. Such samples include a vertically aligned forest of carbon nanotubes grown by CVD methods and several unaligned SWNT films made by arc discharge and HiPco methods, separated by electronic type. All-optical injection and control of such photocurrents was observed in all samples via the emitted THz radiation. Peak current densities in graphite are comparable to that of InP and GaAs; however, the current decays more rapidly with depth due to the high SPA of both the ω and the 2ω beams. In the aligned V-SWNT sample, a peak current of ~8 nA per nanotube is estimated.

A pump polarization study of the current in bulk graphite yielded the injection tensor element ratio $\eta_{xyyx}/\eta_{xxxx} \approx -0.19$, which differs from the value of -1 predicted by Mele *et al.*[28] for graphene, using a tight-binding model with isotropic bands and low-energy photon excitation. A similar study of the aligned V-SWNT sample at two different sample orientations not only gave $\eta_\perp/\eta_\parallel \approx -0.025$, but also gave information on the birefringence of the sample, $\alpha^\parallel/\alpha^\perp \approx 17.9$ and $t^\parallel/t^\perp \approx 1.01$. A polarization study on the unaligned arc discharge semiconducting sample revealed behavior matching that expected for an unaligned ensemble sample and a value of $\eta_\perp/\eta_\parallel \approx -0.068$.

The dependence of the injected current on pump wavelength was measured for second-harmonic wavelengths between 660 and 980 nm for both arc discharge and HiPco X-SWNT samples. For the semiconducting nanotubes, this dependence revealed broad features that peaked at wavelengths different from the linear absorption peaks that are based on exciton transitions. A model was developed to estimate the pump wavelength dependence of the injection current in the semiconducting SWNT films, and qualitative comparisons seem to support the hypothesis that the current injection occurs at energies representing band-band transitions and not excitonic transitions. From this and a theoretical discussion of exciton symmetries, we suggest that the injection current is based on band-band electronic transitions and not excitonic effects. This is significant because it is known that most of the linear optical effects in carbon nanotubes are governed by excitons, and, therefore, this injection current, based on a particular nonlinear process, represents an important exception.

ACKNOWLEDGMENTS

The authors would like to thank Paul Finnie, National Research Council (Ottawa, Canada), for providing the aligned carbon nanotube sample. Thanks to Markus Betz for useful discussions and experimental maintenance. Ilya Gourevich at the Centre for Nanostructure Imaging at the University of Toronto performed SEM measurements. The authors acknowledge financial support generously provided by NSERC, the National Science Foundation, and the Nanoelectronics Research Initiative. R.W.N. acknowledges additional support from the Walter C. Sumner Foundation.

---

[1] L. Huang, Z. Jia, and S. O'Brien, J. Mater. Chem. **17**, 3849 (2007).

[2] K. F. Mak, M. Y. Sfeir, Y. Wu, C. H. Lui, J. A. Misewich, and T. F. Heinz, Phys. Rev. Lett. **101**, 196405 (2008).

[3] Y. B. Zhang, Y.-W. Tan, H. L. Stormer, and P. Kim, Nature (London) **438**, 201 (2005).

[4] K. S. Novoselov, A. K. Geim, S. V. Morozov, D. Jiang, Y. Zhang, S. V. Dubonos, I. V. Grigorieva, and A. A. Firsov, Science **306**, 666 (2004).

[5] F. Xia, T. Mueller, Y. Lin, A. Valdes-Garcia, and P. Avouris, Nat. Nanotechnol. **4**, 839 (2009).

[6] H. Zhang, D. Y. Tang, L. M. Zhao, Q. L. Bao, and K. P. Loh, Opt. Express **17**, 17630 (2009).

[7] T. Dürkop, S. A. Getty, E. Cobas, and M. S. Fuhrer, Nano Lett. **4**, 35 (2004).

[8] S. J. Kang, C. Kocabas, T. Ozel, M. Shim, N. Pimparkar, M. A. Alam, S. V. Rotkin, and J. A. Rogers, Nat. Nanotechnol. **2**, 230 (2007).

[9] M. Engel, J. P. Small, M. Steiner, M. Freitag, A. A. Green, M. C. Hersam, and P. Avouris, ACS Nano **2**, 2445 (2008).

[10] B. L. Allen, P. D. Kichambare, and A. Star, Adv. Mater. **19**, 1439 (2007).

[11] A. Bachtold, P. Hadley, T. Nakanishi, and C. Dekker, Science **294**, 1317 (2002).

[12] W. J. Yu, U. J. Kim, B. R. Kang, I. H. Lee, E.-H. Lee, and Y. H. Lee, Nano Lett. **9**, 1401 (2009).

[13] A. Cottet, T. Kontos, S. Sahoo, H. T. Man, M.-S. Choi, W. Belzig, C. Bruder, A. F. Morpurgo, and C. Schönenberger, Semicond. Sci. Technol. **21**, S78 (2006).

[14] M. S. Purewal, B. H. Hong, A. Ravi, B. Chandra, J. Hone, and P. Kim, Phys. Rev. Lett. **98**, 186808 (2007).

[15] H. B. Heersche, P. Jarillo-Herrero, J. B. Oostinga, L. M. K. Vandersypen, and A. F. Morpurgo, Nature (London) **446**, 56 (2007).

[16] E. J. H. Lee, K. Balasubramanian, R. T. Weitz, M. Burghard, and K. Kern, Nat. Nanotechnol. **3**, 486 (2008).

[17] I. Franco, M. Shapiro, and P. Brumer, Phys. Rev. Lett. **99**, 126802 (2007).

[18] Y. V. Pershin and C. Piermarocchi, Phys. Rev. B **75**, 035326 (2007).

[19] E. Dupont, P. B. Corkum, H. C. Liu, M. Buchanan, and Z. R. Wasilewski, Phys. Rev. Lett. **74**, 3596 (1995).

[20] A. Haché, Y. Kostoulas, R. Atanasov, J. L. P. Hughes, J. E. Sipe, and H. M. van Driel, Phys. Rev. Lett. **78**, 306 (1997).

[21] D. Côté, J. M. Fraser, M. DeCamp, P. H. Bucksbaum, and H. M. van Driel, Appl. Phys. Lett. **75**, 3959 (1999).

[22] L. Costa, M. Betz, M. Spasenović, A. D. Bristow, and H. M. van Driel, Nat. Phys. **3**, 632 (2007).

[23] D. H. Marti, M.-A. Dupertuis, and B. Deveaud, Phys. Rev. B **72**, 075357 (2005).

[24] H. T. Duc, T. Meier, and S. W. Koch, Phys. Rev. Lett. **95**, 086606 (2005).

[25] M. J. Stevens, A. L. Smirl, R. D. R. Bhat, A. Najmaie, J. E. Sipe, and H. M. van Driel, Phys. Rev. Lett. **90**, 136603 (2003).

[26] J. Hübner, W. W. Rühle, M. Klude, D. Hommel, R. D. R. Bhat, J. E. Sipe, and H. M. van Driel, Phys. Rev. Lett. **90**, 216601 (2003).

[27] P. Král and D. Tománek, Phys. Rev. Lett. **82**, 5373 (1999).

[28] E. J. Mele, P. Král, and D. Tománek, Phys. Rev. B **61**, 7669 (2000).

[29] R. W. Newson, J.-M. Menard, C. Sames, M. Betz, and H. M. van Driel, Nano Lett. **8**, 1586 (2008).

[30] D. Sun, C. Divin, J. Rioux, J. E. Sipe, C. Berger, Walt A. de Heer, P. N. First, and T. B. Norris, Nano Lett. **10**, 1293 (2010).

[31] F. Wang, G. Dukovic, L. E. Brus, and T. F. Heinz, Science **308**, 838 (2005).

[32] R. D. R. Bhat and J. E. Sipe, e-print arXiv:cond-mat/0601277 (unpublished).

[33] C. Sames, J.-M. Ménard, M. Betz, A. L. Smirl, and H. M. van Driel, Phys. Rev. B **79**, 045208 (2009).

[34] D. Côté, Ph.D. thesis, University of Toronto, Toronto, 2003.

[35] C. Aversa and J. E. Sipe, IEEE J. Quantum Electron. **32**, 1570 (1996).

[36] P. N. Butcher and D. Cotter, *The Elements of Nonlinear Optics* (Cambridge University Press, Cambridge, U.K., 1990).

[37] R. W. Newson, Ph.D. thesis, University of Toronto, Toronto, 2010.

[38] M. S. Dresselhaus, G. Dresselhaus, R. Saito, and A. Jorio, Ann. Rev. Phys. Chem. **58**, 719 (2007).

[39] I. Rumyantsev and J. E. Sipe, Phys. Rev. B **73**, 201302 (2006).

[40] E. B. Barros, A. Jorio, G. G. Samsonidze, R. B. Capaz, A. G. S. Filho, J. M. Filho, G. Dresselhaus, and M. S. Dresselhaus, Phys. Rep. **431**, 261 (2006).

[41] M. S. Arnold, A. A. Green, J. F. Hulvat, S. I. Stupp, and M. C. Hersam, Nat. Nanotechnol. **1**, 60 (2006).

[42] A. A. Green and M. C. Hersam, Nano Lett. **8**, 1417 (2008).

[43] E. Malić, M. Hirtschulz, F. Milde, A. Knorr, and S. Reich, Phys. Rev. B **74**, 195431 (2006).

[44] M. S. Arnold, A. A. Green, J. F. Hulvat, S. I. Stupp, and M. C. Hersam, Nat. Nanotechnol. **1**, 60 (2006).

[45] X. Tu, S. Manohar, A. Jagota, and M. Zheng, Nature (London) **460**, 250 (2009).

[46] S. Ghosh, S. M. Bachilo, and R. B. Weisman, Nat. Nanotechnol. **5**, 443 (2010).

[47] In a collaboration with B. Weisman,[48] we found our unsorted HiPco SWNTs actually contain a 60% to 40% semiconducting to metallic ratio. The difference is probably due to the decreased set of possible SWNT chiralities in this diameter range. For the larger diameter arc discharge material, the statistical 2 : 1 ratio holds.

[48] A. V. Naumov, O. A. Kuznetsov, A. R. Harutyunyan, A. A. Green, M. C. Hersam, D. E. Resasco, P. N. Nikolaev, and R. B. Weisman, Nano Lett. **9**, 3203 (2009).

[49] Unfortunately, over time the SWNT films tend to lose their adhesion to the glass substrate and begin to flake off. At the time of these height profile measurements, the AD U-X-SWNT sample was compromised, and it was not possible to measure an accurate value of film thickness.

[50] A. Borghesi and G. Guizzetti, in *Handbook of Optical Constants of Solids*, edited by E. D. Palik (Academic, Boston, 1991), Vol. II.

[51] B. S. Wherrett, J. Opt. Soc. Am. B **1**, 67 (1984).

[52] D. Côté, J. E. Sipe, and H. M. van Driel, J. Opt. Soc. Am. B **20**, 1374 (2003).

[53] O. J. Glembocki and H. Piller, in *Handbook of Optical Constants of Solids*, edited by E. D. Palik (Academic, Boston, 1985), Vol. I.

[54] D. F. Edwards and R. H. White, in *Handbook of Optical Constants of Solids*, edited by E. D. Palik (Academic, Boston, 1991), Vol. II.

[55] M. J. Weber, *Handbook of Optical Materials* (CRC, Boca Raton, FL, 2003).